# Effects of volcano loading on dike propagation in an elastic half-space

Jordan R. Muller

Department of Geological and Environmental Sciences, Stanford University, Stanford, California

Garrett Ito

Department of Geology, University of California, Davis, California

Stephen J. Martel

Department of Geology and Geophysics, University of Hawaii at Manoa, Honolulu, Hawaii

**Abstract.** We use laboratory experiments and numerical models to examine the effects of volcano loading on the propagation of buoyant dikes in a two-dimensional elastic half-space. In laboratory experiments we simulate the propagation of buoyant dikes in an isotropic regional stress field by injecting air into tanks of solidified gelatin. A weight resting on the surface of the gelatin represents a volcanic load. A numerical model is used to simulate these experiments. Both experiments and numerical simulations show that as a dike ascends, it begins to curve toward the load in response to the local stress field imposed by the load. The lateral distance over which dikes curve to the load increases with the ratio of average pressure at the base of the load to the dike driving pressure. For realistic volcano and dike dimensions this pressure ratio is going to be large, suggesting that dikes can converge to a volcano over lateral distances several times the load width. Numerical calculations involving an anisotropic regional stress field, however, predict that the lateral extent of dike attraction shrinks as the regional horizontal compressive stress decreases relative to the vertical compressive stress. Dike focusing will be substantial if the regional differential stresses are less than the average pressure at the base of the load. If this is the case, then our models predict a positive feedback between the size of volcanoes and the area of dike attraction. This feedback may promote the development of large discrete volcanoes and also predicts a positive correlation between the spacing and sizes of adjacent volcanoes. To test this prediction, we examine nearest-neighbor pairs of the 21 largest volcanoes in the Cascade Range. The 14 pairs examined show a large range in volcano spacing (6–115 km) and a statistically significant correlation between spacing and average volcano height. This result is consistent with our model results and suggests that the local compressive stress induced by these volcanoes may be an important factor in controlling magma transport in the lithosphere.

## 1. Introduction

The geometry of the subterranean "magma plumbing" in a volcanic province must to a large degree control the distribution, growth rate, and longevity of activity of individual volcanoes. For large volcanoes to form and for eruptions to persist, magma must be focused as it rises from a broad source region at depth to a localized eruption site at the surface [*Decker*, 1987]. In settings where the lithosphere is thin, such as near mid-ocean ridges, magma transport and focusing might be dominated by porous flow in the asthenosphere with flow through fractures, or dikes, occurring close to the surface [e.g., *Turcotte and Phipps Morgan*, 1992]. In contrast, where the elastic lithosphere is thicker, such as in continental or old oceanic settings, dikes may be the

dominant transport mechanism to much greater depths [*Spence and Turcotte*, 1985, 1990; *Rubin*, 1993]. Several mechanisms have been suggested for the focusing of dikes, including the mechanical interaction of propagating dikes [*Takada*, 1994; *Ito et al.*, 1997], lithospheric flexure due to volcano loading [*ten Brink*, 1991], as well as flexure combined with melt-induced erosion of the lithosphere [*Hieronymous and Bercovici*, 1999].

Gravity supplies the vertical force for buoyant dikes to rise, but the direction of propagation is not necessarily vertical as it is controlled by the stress field near the upper dike tip [*Pollard and Segall*, 1987] as well as preexisting structures [*Delaney et al.*, 1986]. The near-tip stress field in turn is controlled by dike pressure and dike geometry, as well as the ambient stress field which includes effects of volcano loads. The studies of *ten Brink* [1991] and *Hieronymous and Bercovici* [1999] utilize thin plate theory, which considers variations in horizontal stress due to bending but not variations in vertical stress. As a result, these studies can not be used directly to predict the propagation direction of dikes.
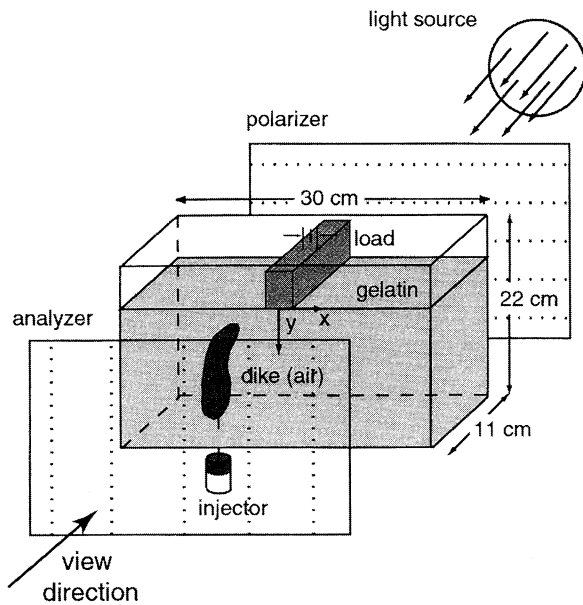
**Figure 1.** Sketch of the experimental apparatus showing the surface load and the injection of air dikes at the tank base. The polarization directions of two polarizing sheets are aligned orthogonally on either side of the tank (indicated by dotted lines). A white light source shines through the back of the tank to illuminate the photoelastic stress pattern in the gelatin.

*Jackson*, 1972; *Takada*, 1990, 1994; *Heimpel and Olson*, 1994; *Ito et al.*, 1997]. We use 250A ordnance grade gelatin from the Kind and Knox Company, prepared at weight percent of 1.5% for all experiments. The shear modulus $\mu$ of this concentration was determined to be $444 \pm 88$ Pa based on comparisons of laboratory and theoretical dike shapes. Poisson's ratio is ~ 0.5.

To simulate a volcanic load, we place a rigid rectangular weight on the gelatin surface in the middle of the tank and aligned with short horizontal dimension of the tank. The load has a half width $l$ of $1.6\times10^{-2}$ m and a length of $10.2\times10^{-2}$ m. The mass of the load is varied from $4.5\times10^{-2}$ kg to $12.5\times10^{-2}$ kg to yield average load pressures of $P_{load} = 135\text{-}375$ Pa. The $x$ coordinate is the horizontal distance from the center of a surface load, as measured parallel to the long axis of the tank (Figure 1). The $y$ axis is vertical, with $y$ equal to zero at the surface of the gelatin and becoming more negative with depth.

Dikes are injected at the tank base through silicone-sealed holes spaced 1 cm apart along a line parallel to the long axis of the tank. To initiate each dike vertically and perpendicular to the $x$ axis, a small slit is cut with the tip of a syringe. We use air as the dike fluid because its low viscosity and large density contrast with the gelatin minimize the dike size required for sufficiently high propagation rates. All dikes are injected with an air volume of $2.5\times10^{-6}$ m$^3$. The dikes grow spontaneously to an average steady state head length $L$ of $3.5\times10^{-2}$ m and a maximum width $W_0$ of ~$0.6\times10^{-2}$ m (Figure 2) and propagate to the surface. We inject dikes individually with increasing distance $x$ away from the load. To minimize
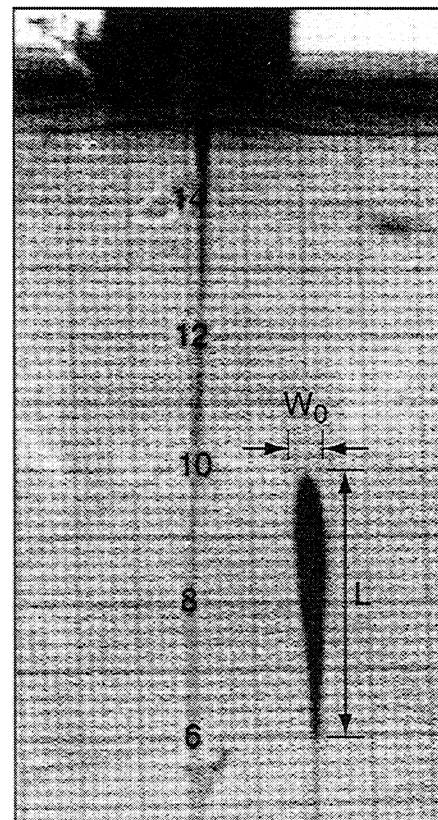
To quantify the effects of a volcanic load on the propagation direction of dikes, we use a combination of laboratory experiments and numerical models. We examine two-dimensional (2-D) stress solutions in an elastic half-space. The half-space approach simplifies the problem and is most suitable for small loads on thick lithosphere. In laboratory experiments, air-filled dikes are injected into a tank of solidified gelatin. A load applied on the gelatin surface causes dikes to curve toward the load; the lateral distance over which dikes are attracted depends on the load magnitude, load width, and dike driving pressure. We then use numerical models to examine the mechanics of the laboratory experiments and to analyze the potential for dike attraction for a range of natural loads, dike sizes, and regional stresses in the lithosphere. The feedback between volcano size and region of dike attraction is predicted to result in a correlation between size and spacing of volcanoes within a volcanic province. We close by testing this prediction by analyzing sizes and spacing of the largest volcanoes in the Cascade Range of the western United States.

## 2. Laboratory Experiments

### 2.1. Experimental Method and Observations

The experiments are designed to investigate the propagation of dikes in a 2-D elastic half-space. As shown in Figure 1, the experimental apparatus includes a gelatin-filled tank with a Plexiglas base, a pair of polarizing sheets, the surface load, and a syringe used to inject the dikes. Gelatin has a small fracture toughness and is transparent, so fractures are easy to initiate, propagate, and observe; it has therefore been used in a number of studies of dike mechanics [e.g., *Fiske and*



**Figure 2.** Photograph of an experimental air-filled dike during propagation. The bold grids are centimeters, and narrow grids are 0.2 mm. The load and dike are shown in cross section. The dike height $L$ is ~3.8 cm.
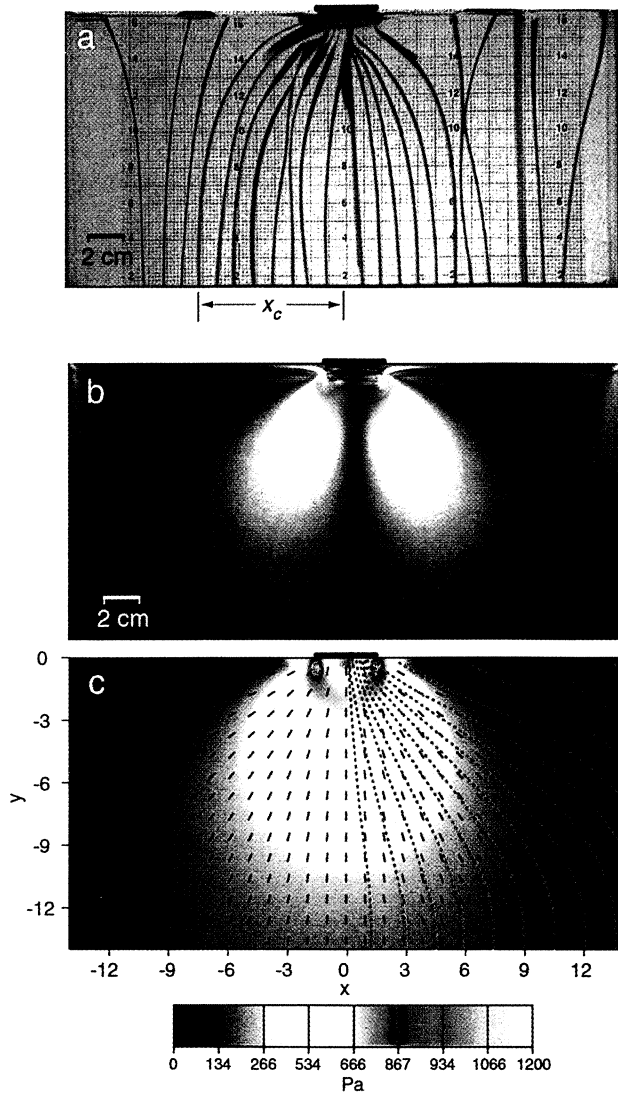
Plate 1. (a) After completion of the experiment, with propagation paths dyed green to highlight the trajectories of the buoyant dikes. (b) Photoelastic stress field induced by a $9.9 \times 10^{-2}$ kg flat surface load (black bar at top center), $P_{load} = 297$ Pa. Colors reflect the magnitude of the differential stress within the gelatin. (c) Numerically calculated differential stress contours and most compressive principal stress trajectories beneath a load of the same size and magnitude. Note that the location of vertical stress trajectories, at $x = 0$, corresponds to the location of the dark vertical band (isogyre) at $x = 0$ in Plate 1b. Red dots indicate dike paths predicted by numerical models of dike propagation in this stress field.

the influence of previous dike injection, each dike is allowed to "erupt" at the gelatin surface and close before injection of the next dike. Approximately 18 dikes are injected per experiment.

We find that initially the dikes rise nearly vertically (i.e., in the direction they are initiated, thus indicating that propagation paths are influenced little by the injection depth). As the dikes approach the surface load, however, they begin to curve towards the load (Plate 1a). As the dikes rise closer to the load, their lengths $L$ decrease and their widths $W_0$ increase slightly. We also find that only those dikes injected within a critical lateral distance $x_c$ from the load center actually

intersect the base of the load, whereas those dikes injected at a distance greater than $x_c$ curve little as they propagate and fail to reach the load.

In addition to dike paths we also image the pattern of stresses in the gelatin using the gelatin's photoelastic properties. To do this, polarizing sheets are placed orthogonally on either side of the tank (Figure 1). White light is directed through the back polarizer, into the tank, and out through the front polarizing sheet. If the gelatin is stressed, then an interference pattern is produced that represents the magnitude of differential stresses $(\sigma_1 - \sigma_3)$ [*Timoshenko and Goodier*, 1970] (note that in this paper, we adopt the convention that compressive stresses are positive). In the absence of a surface load the photoelastic field is uniformly dark, indicating that the initial stress state in the gelatin is isotropic; dikes do not curve as they propagate under these conditions. Once a load is applied, photoelastic fringes appear (Plate 1b), indicating the presence of differential stresses. A bright region beneath the load denotes high differential stresses. The fringe pattern decreases in intensity with radial distance from the load, reflecting an associated decrease in the differential stresses. The dark region separating the two bright lobes in Plate 1b is an isogyre. It does not reflect differential stress magnitude but instead shows where light fails to penetrate the system because the orientations of the principle stresses coincide with the orientations of the crossed polarizing sheets (i.e., horizontal and vertical).

Below we define pressure and length scales that enable us to compare laboratory experimental results to those of numerical models and to make predictions of the behavior of natural dikes beneath real volcanoes. One aspect of our laboratory experiments, however, cannot be scaled appropriately to dikes in the Earth. In our experiments the stress intensity factor $K_I$ at upper tip of the dikes is less than the fracture toughness of the gelatin. This fact is evident in the low ascent rates (0.003
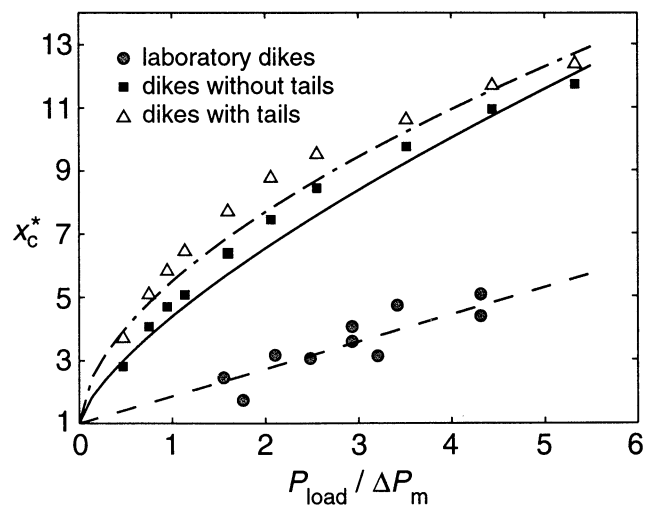


Figure 3. Relationship between $x_c$ and the ratio of the average surface load stress $(P_{load})$ and the midheight dike driving pressure $(\Delta P_m)$. Dashed line shows the best fit line (equation (2)) passing through the experimental data (circles) and the point (0,1), the solid line (equation (6)) fits data from corresponding numerical experiments of dikes without tails (squares), and the dot-dashed line (equation (7)) fits numerical experiments of dikes with open tails (triangles).
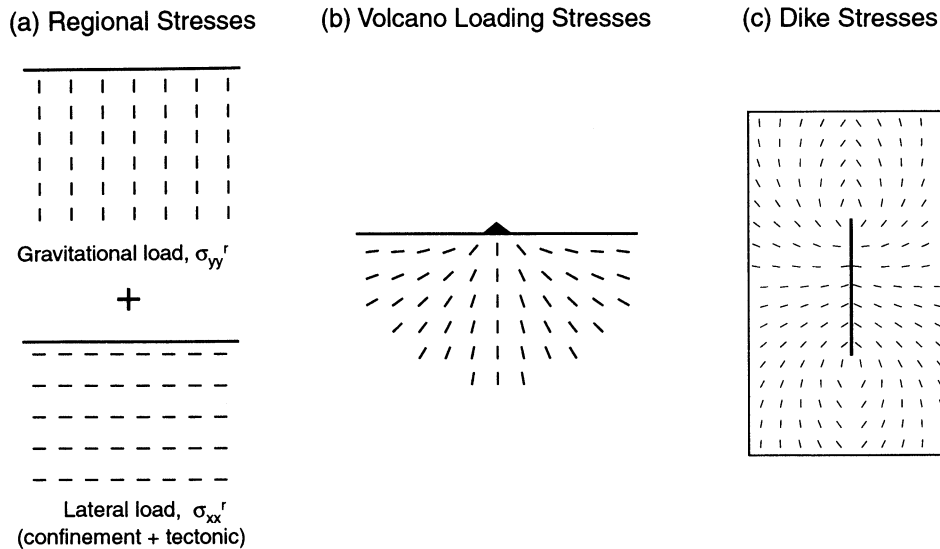
### (a) Regional Stresses     (b) Volcano Loading Stresses     (c) Dike Stresses

Gravitational load, $\sigma_{yy}{}^r$

**+**

Lateral load, $\sigma_{xx}{}^r$
(confinement + tectonic)

**Figure 4.** The three contributions to the stress field beneath a volcano: (a) regional stresses composed of a vertical gravitational component and a horizontal tectonic component, (b) a radial volcanic component, and (c) a perturbation due to the dike.

m s$^{-1}$) of the gelatin dikes and an observed exponential increase in ascent velocity with increasing $K_I$ (such subcritical propagation in gelatin is analyzed in more detail by *Heimpel and Olson* [1994]). The low propagation rate and the low viscosity of the dike fluid result in a minimal driving pressure drop along the dike due to flow of air as this dike rises. As a consequence, elastic stresses balance with buoyancy of the dike fluid to achieve momentum equilibrium. In the Earth, by contrast, the fracture toughness of host rock is exceeded by magma-filled dikes of minimal height (~$10^2$ m) and width (~$10^{-3}$ m) [*Lister and Kerr*, 1991]. Dike ascent rate is therefore limited by magma viscosity, and equilibrium is achieved by a balance of magma fluid stresses and magma buoyancy [e.g., *Spence and Turcotte*, 1985; *Lister*, 1990; *Lister and Kerr*, 1991; *Rubin*, 1995].

The above discrepancy between our laboratory and natural dikes produces differences in pressure distribution along the dikes. Buoyant dikes can be considered as consisting of two parts: a dike head of nearly constant length along which driving pressures are largest and a tail with minimal driving pressure that lengthens below the head during propagation. We later refer to a special kind of dike, a Weertman dike [*Rubin*, 1998], that only has a head. A Weertman dike is a buoyant dike that moves upward, even in the absence of additional magma influx, by fracturing at the top and squeezing shut at the bottom. The head of our laboratory dikes contains nearly the entire volume of injected air (Figure 2). The head maintains a linear driving pressure distribution much like that of a stationary Weertman dike [*Secor and Pollard*, 1975; *Pollard and Muller*, 1976]. This is similar to buoyant dikes in the Earth, which are predicted to also have an approximately linear pressure distribution along most of the dike head, although the pressure gradient changes with dike volume [*Rubin*, 1995]. The tail of our laboratory dikes narrows such that substantial portions appear to close (the walls have relief and are not perfectly flat), and therefore the tail may support stresses much like the gelatin. Isolated natural dikes, on the other hand, are predicted to have a more

even distribution of magma between the head and tail, and the driving pressure in the tail is predicted to be near zero [*Rubin*, 1998]. Considering these factors, our laboratory experiments apply most directly to natural dikes of volume small enough to produce a head with a driving pressure close to that of a static dike [see *Rubin*, 1998, Figure 3] and a tail capable of supporting stresses much like the host rock. The latter condition could be met if a substantial area of the tail walls close or if magma in the tail freezes. For the sake of completeness we treat both closed and open dike tails in our analyses.

### 2.2. Experimental Results

Here we derive a scaling law that relates the maximum distance from which surface loads attract dikes $x_C$ to three key parameters: the load half width $l$, the average load stress $P_{load}$, and the dike driving pressure at the midheight of the dike head $\Delta P_m$. The distance $x_c$ is the $x$ position of the base of the outermost dike to reach the surface load (Plate 1a). We scale $x_c$ by the load half width $l$ to define a dimensionless critical distance $x^*_c$ (see Table 1 for definition of all variables). We scale the average pressure at the base of the load $P_{load}$ by a characteristic dike driving pressure $\Delta P_m$, which we define as the difference in dike fluid pressure and the isotropic pressure in the gelatin at the midheight of the dike's head. On the basis of the analysis of *Secor and Pollard* [1975] on 2-D buoyant dikes on the verge of propagation

$$\Delta P_m = \Delta \rho g L/4. \tag{1}$$

Here, $\Delta \rho = 1015$ kg m$^{-3}$ is the density contrast between the host material (the gelatin) and the dike fluid (air), and $g = 9.8$ m s$^{-2}$ is the acceleration of gravity. Equation (1) indicates that changes in a dike's length $L$ during propagation would change the midheight driving pressure. In the experiments we found this length change to be minimal (<10%) and therefore assume that the midheight dike head driving pressure remains constant.

**Table 1.** Notation

| Parameter | | Units |
|---|---|---|
| $A_{ij}$ | matrix of influence coefficients | Pa m$^{-1}$ |
| $B_j$ | stress on boundary element | |
| $D$ | flexural rigidity | |
| $E$ | Young's modulus | Pa |
| $g$ | acceleration of gravity | m s$^{-2}$ |
| $h$ | maximum volcano height | m |
| $k$ | regional stress factor | |
| $K_I$ | opening-mode stress intensity | Pa m$^{1/2}$ |
| $K_{II}$ | shear mode stress intensity | Pa m$^{1/2}$ |
| $l$ | half width of the load | m |
| $L$ | dike length | m |
| $n$ | number of volcano pairs | |
| $P$ | pressure along the dike | Pa |
| $P_0$ | dike pressure term used to account for surface load | Pa |
| $P_{load}$ | average normal stress of load | Pa |
| $P_{max}$ | maximum normal stress of load | Pa |
| $\Delta P_m$ | driving pressure at midheight of the dike head | Pa |
| $r$ | correlation coefficient | |
| $t$ | statistical test parameter | |
| $T_e$ | effective elastic thickness of the lithosphere | m |
| $V_0$ | applied surface load magnitude | Pa m |
| $w$ | deflection of elastic plate beneath a line load | m |
| $W_0$ | maximum dike width | m |
| $x$ | horizontal position relative to the load center | m |
| $x_c$ | distance of dike attraction | m |
| $x^*_c$ | dimensionless distance of dike attraction | |
| $X_i$ | displacement discontinuities on boundary element | m |
| $y$ | depth beneath the surface and base of load | m |
| $y_m$ | depth of dike center | m |
| $\alpha$ | flexural wavelength | m |
| $\eta$ | viscosity | Pa s |
| $\nu$ | Poisson's ratio | |
| $\mu$ | shear modulus | Pa |
| $\rho_l$ | load density | kg m$^{-3}$ |
| $\rho_0$ | ambient lithosphere density | kg m$^{-3}$ |
| $\Delta\rho$ | density contrast between dike fluid and ambient | kg m$^{-3}$ |
| $\sigma_1$ | maximum principle compressive stress | Pa |
| $\sigma_3$ | minimum principle compressive stress | Pa |
| $\sigma^f_{max}$ | maximum horizontal stress of a flexed elastic plate | Pa |
| $\sigma^f_{xx}$ | horizontal stress within a flexed elastic plate | Pa |
| $\sigma^r_{xx}$ | regional horizontal compressive stress | Pa |
| $\sigma^r_n$ | regional normal stress along the dike | Pa |
| $\sigma^r_{xy}$ | regional shear stress | Pa |
| $\sigma^r_{yy}$ | regional vertical compressive stress | Pa |
| $\tau_a$ | viscous relaxation time | years |

Experimental values of $x^*_c$ are plotted in Figure 3 as a function of the ratio $P_{load}/\Delta P_m$ (circles). The experimental values of $x^*_c$ are well described as a linear function of $P_{load}/\Delta P_m$,

$$x^*_c = 0.86(P_{load}/\Delta P_m) + 1 \qquad (2)$$

(in deriving the coefficient of 0.86 we found the best fit slope while constraining the intercept to be 1). This relation indicates (1) that for a surface load of zero, only dikes injected within one load half width of the load centerline will intersect the load and (2) that increasing surface loads will attract dikes from greater lateral distances.

## 3. Numerical Experiments

### 3.1. Dike Mechanics

Dikes are opening-mode fractures that propagate normal to the direction of minimum compression ($\sigma_3$) ahead of the dike tip [Ingraffea, 1987; Pollard and Segall, 1987]. In two dimensions, propagation is in the direction of the maximum compression ($\sigma_1$). The stress field near the tip of a dike has contributions from three main sources (Figure 4). The first source is the regional, or far-field, stress (Figure 4a). If the vertical ($\sigma^r_{yy}$) and horizontal ($\sigma^r_{xx}$) components of the regional stress field are the principal stresses and are equal, the stress state is isotropic; if the differential stresses are nonzero, then the stress field is anisotropic. In this paper, we will analyze the propagation of dikes in both isotropic and anisotropic regional stress conditions. The second contribution is from the load of the volcano (Figure 4b). In an elastic half-space the most compressive stresses due to a surface load will tend to form an approximately radial pattern [Johnson, 1985]. We refer to the stress field formed by superposing the regional and the volcano load contributions as the ambient field. The third contribution is the stress perturbation associated with the dike itself (Figure 4c).

If the differential stress of the ambient field is substantially greater than the dike driving pressure, then the dike will propagate along the most compressive stress direction of the ambient stress field [Olson and Pollard, 1989], provided a preexisting anisotropy or weakness is absent. On the other hand, if ambient differential stresses are small compared to the dike driving pressure, then the stress field produced by opening of the dike walls dominates near the dike tip and the dike will propagate essentially in-plane. Finally, if the magnitudes of the ambient differential stress and the dike driving pressure are similar, then a dike that is oriented obliquely with respect to $\sigma_1$ will tend to curve gradually as it
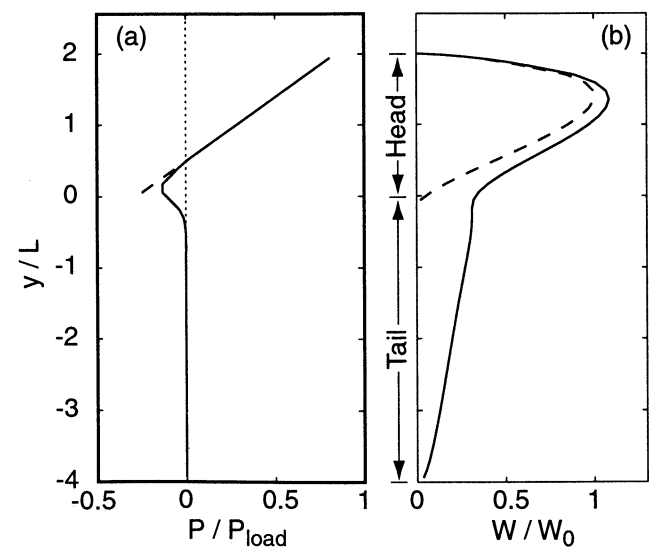


**Figure 5.** (a) Normalized pressure in dike without a tail (dashed) and with an open tail (solid) as a function of vertical distance normalized by the length of the dike head ($L$). (b) Half thickness of dike with and without tails (solid and dashed, respectively) for corresponding pressure distributions in Figure 5a. The term $W_0$ is the maximum dike thickness.

a) $(1-k)\rho_0 gl/P_{load} = -0.743$



b) $(1-k)\rho_0 gl/P_{load} = 0.371$



c) $(1-k)\rho_0 gl/P_{load} = 0.743$



0.0    0.4    0.8    1.2    1.6    2.0    2.4    6.8
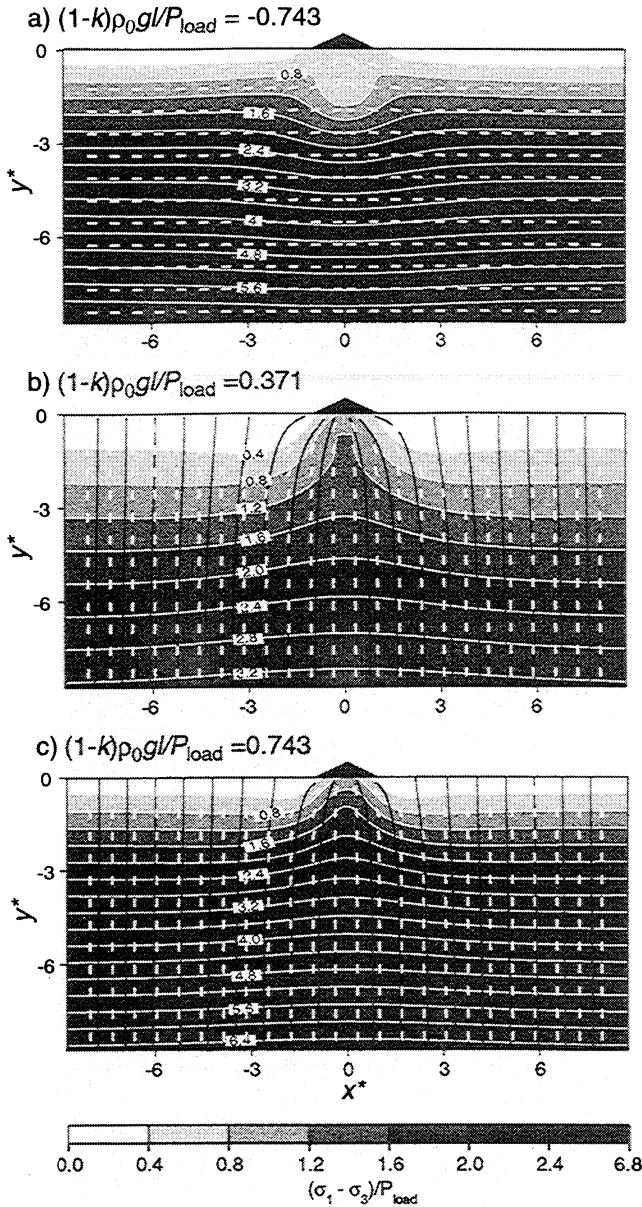
$(\sigma_1 - \sigma_3)/P_{load}$

**Figure 6.** Magnitude of scaled differential stress (shaded and contoured), trajectories of the most compressive principal stress (ticks), and potential dike propagation paths (solid lines) beneath a triangular normal load distribution for a regional differential stress that increases with depth. Differential stress parameter $(1-k)\rho_0 gl/P_{load}$ is equal to (a) -0.743, (b) 0.371, and (c) 0.743.

propagates before becoming parallel to $\sigma_1$ [*Emerman and Marrett*, 1990]. Thus the directions in which the dikes are likely to propagate will be a function of the dike driving pressure and the ambient principal stress magnitudes and orientations. This is consistent with the observed dependence of $x_c$ on $\Delta P_m$, $P_{load}$, and $l$ in Figure 3.

### 3.2. Numerical Simulations of Laboratory Experiments

Here we use a numerical method to examine how the above stress contributions influence dike focusing beneath volcanoes. We start by simulating the gelatin experiments, which have an isotropic remote stress, and then extend the

models to consider cases in which the regional stress field is anisotropic.

The boundaries of the elastic body in the model include the surface of the elastic material as well as any dike walls. These boundaries are approximated by a series of elements with constant displacement discontinuities. Using influence coefficients $A_{ij}$ derived from the analytical solution for a single displacement discontinuity, the method we employ (TWODD [*Crouch and Starfield*, 1983]) relies on the principle of superposition to solve for the displacement discontinuity $X_i$ at each boundary element such that the prescribed stress conditions $B_j$ are met for each element:

$$[A_{ij}][X_i]=[B_j]. \tag{3}$$

The displacement discontinuities $X_i$ can then be used to calculate stresses and displacements at any point within the body.

We idealize the body of gelatin as a 2-D elastic half-space. We treat the "regional stresses" within the gelatin with the following far-field boundary conditions:

$$\sigma_{yy}{}^r = \rho gy; \quad \sigma_{xy}{}^r = 0; \quad \sigma_{xx}{}^r = k\sigma_{xx}{}^r, \tag{4}$$

where $k$ is a prescribed constant. Setting $k$ equal to one yields an isotropic stress condition, such as is present within the gelatin prior to surface loading. Compression again is positive.

We numerically simulate the surface of the body with a series of boundary elements extending along $y = 0$ away from the surface load. A total length of 75 times the load half width is sufficient to simulate an infinite surface surrounding the load. To represent the surface load, normal stress boundary conditions are applied such that they produce uniform vertical displacements along the load base [*Johnson*, 1985]. We specified zero shear stress along the load elements because we lubricated the base of the load in the laboratory. Boundary conditions of zero normal and shear stress are applied along the remainder of the surface boundary.

To simulate the laboratory experiments, we first consider dikes with tails that are completely closed. To do this, boundary elements along only the dike head are specified. Along these dike head elements, we prescribe a normal stress boundary condition $P$ that varies according to

$$P = \Delta\rho g(y - y_m) + \Delta P_m + P_0 + \sigma_n{}^r. \tag{5}$$

Element midpoint depth is given by $y$, the middle of the entire dike is at a depth $y_m$, and the remote stress at $y$ is $\sigma_n{}^r$. We approximate the effect of the load by adding a term $P_0$, which is continually updated such that the dike maintains a constant volume as it ascends. The driving pressure function $(\Delta\rho g(y - y_m) + \Delta P_m + P_0)$ yields a tear-shaped dike head (dashed line in Figure 5b), consistent with the laboratory dikes and predictions of *Secor and Pollard* [1975]. The dike walls are prescribed to have no shear stress. Comparable to the experimental dikes, each numerical dike head has a height equal to 1.1 times the surface load width. Dike propagation is carried out incrementally by adding one element to the upper tip of the head and subtracting one element from the lower tip. In this manner the dike length is constant throughout propagation as is generally the case in the gelatin experiments. We assign the orientation of each new element to be that which yields the minimum resolved shear stress along the new element [*Cotterell and Rice*, 1980; *Olson and Pollard*, 1991]. This direction will be approximately normal to the maximum tensile hoop stress about the dike tip.

Plate 1c shows the numerically calculated stress field for the same load as the laboratory experiment in Plates 1a and 1b. The color scheme used in the theoretical stress field (Plate 1c) is designed to simulate the photoelastic image and shows a general pattern of stress similar to the laboratory experiments. The ticks in Plate 1c show the orientation of the most compressive principal stress. All of these trajectories point toward the load, and therefore the numerical dikes curve toward the load (Plate 1c). Differential stresses are predicted to be largest directly beneath the load and to decrease with radial distance away from the load. This prediction is consistent with the photoelastic image (Plate 1b) which shows greatest intensity close to the load (Plate 1b). Both the photoelastic and numerical stress fields account for why the experimental dikes initially propagate vertically and then curve as they approach the load.

Like the laboratory experiments, the numerical models indicate that $x^*_c$ increases in proportion to $P_{load}/\Delta P_m$. The numerical results are best fit by the function

$$x^*_c = 3.38(P_{load}/\Delta P_m)^{0.71} + 1 \qquad (6)$$

(again subject to the constraint that $x^*_c = 1$ for no load). One difference from the scaling law obtained from the laboratory results (equation (2)) is that (6) predicts a nonlinear increase in $x^*_c$ with $P_{load}/\Delta P_m$. Scatter in the laboratory results, however, is too large to resolve any curvature in the observed trend; thus we use a simple linear fit. More importantly, the numerical models predict dikes to reach the load over greater distances $x^*_c$ than the laboratory experiment. This difference is most likely to be due largely to two our 2-D numerical approximation of the 3-D laboratory dikes. While a numerical dike extends infinitely in the out-of-plane direction, the head of a laboratory dike is only approximately as wide as it is tall. Since the shear mode (mode II) stress intensity factor $K_{II}$ will decrease as you move from the upper tip of the head to the sides there may be a reduced tendency for laboratory dikes to curve as compared to the numerical dikes. Both the numerical and laboratory results, however, indicate an increase in connection distance with load pressure and width and a decrease with midheight dike driving pressure.

### 3.3. Simulations of Dikes With Fluid-Filled Tails

We now examine propagation of dikes with tails that remain open. Propagation direction depends on the ratio of the opening-mode ($K_I$) and shear mode ($K_{II}$) stress intensity factors for the upper dike tip [Lawn, 1993]. Because the driving pressure along the tail is likely to be near zero [e.g., Rubin, 1998], it is unlikely to change the opening-mode stress intensity factor ($K_I$) at the upper dike tip. The mode II stress intensity factor, however, may be affected because a tail filled with a viscous fluid may support less shear stress than the surrounding rock. Any shear displacements of the dike walls will contribute to the shear-mode stress intensity ($K_{II}$) at the upper tip and therefore affect the propagation path.

We now add tail elements beneath the dike head. Solving the coupled equations of viscous flow in elastic fractures is inappropriate for this study, and therefore the driving pressure distribution specified along the dike is an approximation to the asymptotic distribution predicted by Rubin [1998] for viscous flow in a dike of constant volume. Figure 5a shows the driving pressure in the dike head ($y/L>0$) and in the dike tail ($y/L<0$). The boundary condition along the upper 75% of the dike head is given in (5). In the lower 25% of the dike head

the driving pressure becomes negative and decreases to a minimum that is 50% of the minimum for the dike without a tail (dashed line). Just below the dike head, the driving pressure tapers to zero. Again, shear stress is zero along the entire dike. We propagate only the upper tip of the dike and keep the lower tip fixed. As a result, the tail below the dike head remains open and lengthens as the head portion ascends (Figure 5b). Note in Figure 5b that the opening profile near the top of a dike head is virtually identical for dikes with and without tails; this is consistent with the tail contributing little to the opening mode stress intensity factor at the tip of the dike head.

Figure 3 (triangles) shows the predicted dependence of $x^*_c$ on $P_{load}/\Delta P_m$. The best fit function is

$$x^*_c = 4.49(P_{load}/\Delta P_m)^{0.57} + 1. \qquad (7)$$

The load of a volcano is able to attract dikes with open tails over greater horizontal distances than the dikes with closed tails. This result is consistent with the anticipated increase in $K_{II}$ associated with the tail. The above results suggest that dike focusing will be even greater for dikes with tails that remain fluid. We note, however, that we have assumed the extreme case in which the tail fluid is perfectly inviscid. Tails filled with viscous fluids will be capable of sustaining shear stress over finite time scales. Thus we may be overpredicting the effects of dike tails on propagation direction.

### 3.4. Realistic Scales

In order to relate the analysis above to the Earth we consider realistic values of $P_{load}$, $\Delta P_m$, and surface load dimensions. The example we consider is Mount Shasta in northern California. Considering Mount Shasta's approximate volume of $3.5 \times 10^{11}$ m$^3$ [Wood and Kienle, 1990] and assuming an average density and basal radius of 2600 kg m$^{-3}$ and $1.3 \times 10^4$ m, respectively, $P_{load}$ is ~17 MPa. To estimate $\Delta P_m$ we consider the range expected of dikes arising from a partially molten source in the mantle. A minimum estimate is made by assuming that $K_I$ at the upper tip of the dike head equals the ambient fracture toughness. For a fracture toughness of 3 MPa m$^{1/2}$ and a density contrast between magma and lithosphere of $\Delta\rho$=300 kg m$^{-3}$, $\Delta P_m$ = 0.15 MPa. This driving pressure corresponds to a Weertman dike that is 200 m tall and 0.78 mm thick (using equations (4) and (5) of Rubin [1998] and assuming an elastic stiffness of 50 GPa). A maximum estimate of $\Delta P_m$ is based on the largest dike heads predicted by Rubin [1998] in his Figure 6. These dikes are fed by porous flow. These dike heads have a midheight driving pressure of ~2 times the value of $\Delta P_m$ for the 200 m tall dike (i.e., ~0.3 Mpa). The dike head fed by porous flow corresponding to this driving pressure is about 12 times the Weertman dike half height (~1200 m tall). Figure 6 and equation (5) of Rubin [1998] give a scaling factor between the Weertman dike maximum thickness and the thickness scale $W$ equal to 14/0.65 or about 20. Multiplying our Weertman dike maximum thickness (0.78 mm) by 20 yields a thickness of 16 mm. Thus for these two different modes of dike growth $P_{load}/\Delta P_m$ is expected to be 50-100. From (2), (6), and (7), this range of pressure ratios predicts values of $x_c$ many times (50-100) the width of the load. Due to thermal considerations, however, we expect this estimate for $x_c$ to be an upper bound. In order to traverse the lithosphere before freezing, dikes would have to be much thicker (~ 1 m) [Lister, 1994] and would likely have a greater driving pressure. The general conclusion is that large

volcanoes are capable of attracting dikes over lateral distances many times their basal width. Even though our analyses are based on 2-D surface loads, we anticipate this conclusion to hold for 3-D volcanic loads provided regional stresses are isotropic.

## 4. Effects of Regional Differential Stresses on Dike Propagation

Several investigators have suggested that tectonic stresses within the lithosphere can affect the distribution of surface eruptions [*Hughes et al.*, 1980; *Rogers*, 1985; *Weaver and Michaelson*, 1985; *Guffanti and Weaver*, 1988]. In this section we examine how a range of anisotropic regional stress states may influence deep focusing of dikes. When the regional stresses are isotropic, as in the above experiments, $k$ = 1 in equation (4). This condition applies best where the mantle or crust deforms viscously over long time periods to alleviate any differential stress [*Anderson*; 1951; *McGarr*, 1988]. This condition, however, is not the only accepted reference state of stress. A reference state of lateral confinement (no horizontal displacement) has also been employed [e.g., *Jaeger and Cook*, 1979; *Savage et al.*, 1985; *McGovern and Solomon*, 1993]. In this case the horizontal normal stress, $\sigma_{xx}^{r}$, is a fraction of the vertical stress, $\sigma_{yy}^{r}$, caused by gravity,

$$\sigma_{xx}^{r} = \left(\frac{\nu}{1-\nu}\right)\sigma_{yy}^{r}, \qquad (8)$$

where $\nu$ is Poisson's ratio. For crustal and mantle rock, where $\nu$ is typically near 0.25, the horizontal stress would be ~1/3 the vertical stress (i.e., $k$ = 1/3). This is a substantial difference from the isotropic condition of (4). Indeed, the existence of thrust faults demonstrates that $\sigma_{xx}^{r}$ can exceed $\sigma_{yy}^{r}$, so $k$ can also exceed one.

We now test the effects that differential regional stresses within the lithosphere would have on the trajectories of buoyant dikes beneath volcanoes. We establish an anisotropic regional stress field by setting $k$ in the range from 0.8 to 1.1. As we will show, this range is sufficient to illustrate the key effects of anisotropic regional stresses. The absolute magnitude of the regional differential stress $|(\sigma_{yy}^{r}-\sigma_{xx}^{r})|$ increases with depth in accord with (4). The dimensionless variable with which we parameterize the results is the regional differential stress at a depth equal to one surficial load half width, normalized by the average magnitude of the surficial load; that is the ratio $(1-k)\rho_0 g l / P_{load}$, in which $\rho_0$ is the density of the lithosphere. The regional stress field is isotropic when the differential stress is zero (i.e., $k$ = 1). To more realistically simulate a volcano load, we apply a triangular distribution of normal compressive stresses at the ground surface

$$P_{load}(x) = \frac{\rho g h(l - |x|)}{l}, \qquad (9)$$

where $|x| \leq l$ and $\rho_l$ is the density of the load. The average normal load stress, $P_{load}$, is $\rho_l g h/2$. The shear stress along the ground surface is set to zero. For simplicity, we assume that dikes track the most compressive stress trajectories; this will be the case where $P_{load}/\Delta P_m$ is very large. This simplification will lead to a slight overestimate of the influence of the load to the degree that $\Delta P_m$ affects dike propagation direction. (For example, in the case of isotropic remote stresses, $x^*_{c}$ will be

infinite. This result, however, would not be a poor approximation of $x^*_{c}$ = ~50, which is predicted from (6) for $P_{load}/\Delta P_m$ = $10^2$.) We use streaklines parallel to the most compressive stress as a proxy for potential dike paths beneath a model volcano. The outermost streakline to reach the load determines $x_c$.

Figure 6 shows differential stress fields $(\sigma_1-\sigma_3)$, normalized by $P_{load}$, for cases in which the regional horizontal compressive stress exceeds the vertical regional compression (Figure 6a) and two cases in which the regional horizontal compression is less than the vertical compression (Figures 6b and 6c). In the Figure 6a the differential stress parameter, $(1-k)\rho_0 g l / P_{load}$ = -0.743. This case corresponds to $k$ = 1.09, $\rho_l/\rho_0$ = 0.87, and a value of $P_{load}$ appropriate for Mount Shasta (17 MPa). The trajectories of most compressive stress are nearly horizontal except for a small region beneath the load. In this case, vertical propagation of buoyant dikes is inhibited by the horizontal compression and an extensive vertical feeder dike system is unlikely to develop. Figures 6b and 6c show cases where the differential stress parameter is 0.371 ($k$ = 0.96, $P_{load}$ = 17 MPa) and 0.743 ($k$ = 0.91, $P_{load}$ = 17 MPa), respectively. A comparison of the two figures shows that as the vertical regional compressive stresses increase relative to the horizontal regional stresses, the vertical gradient in differential stresses increases, and the most compressive stresses as well as the dike trajectories everywhere become more vertical. Thus, as $(1-k)\rho_0 g l / P_{load}$ increases, the regional stress field becomes increasingly important relative to the surface load in controlling dike trajectories.

The relationship between the distance of dike attraction $x^*_{c}$ and differential stress parameter $(1-k)\rho_0 g l / P_{load}$ is summarized in Figure 7. As $(1-k)\rho_0 g l / P_{load}$ increases from 0.0 to ~0.50, the distance of dike attraction $x^*_{c}$ decreases very rapidly. As $(1-k)\rho_0 g l / P_{load}$ increases beyond ~0.50, $x^*_{c}$ decreases more gradually and eventually tapers to an asymptotic value of 1.0. The numerical results are well described by the scaling law
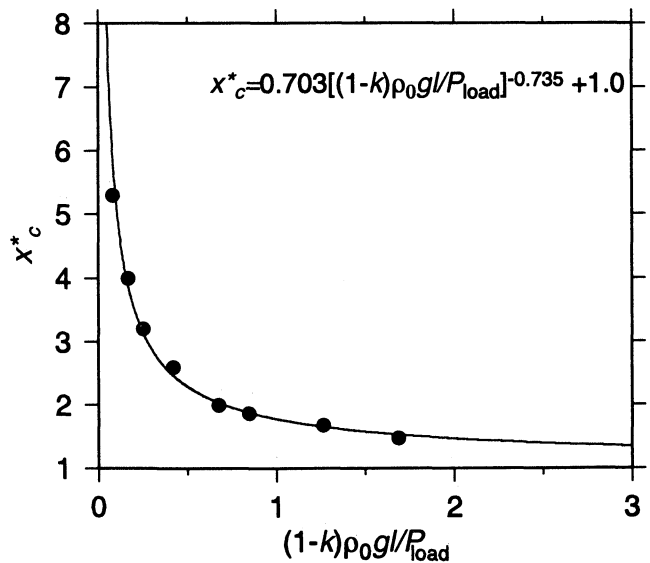
**Figure 7.** The maximum normalized distance that dikes will reach a load $x^*_{c}$ is predicted to decrease with increasing differential stress parameter $(1-k)\rho_0 g l / P_{load}$. The numerical predictions (dots) are well explained by the above relationship (equation (10)).
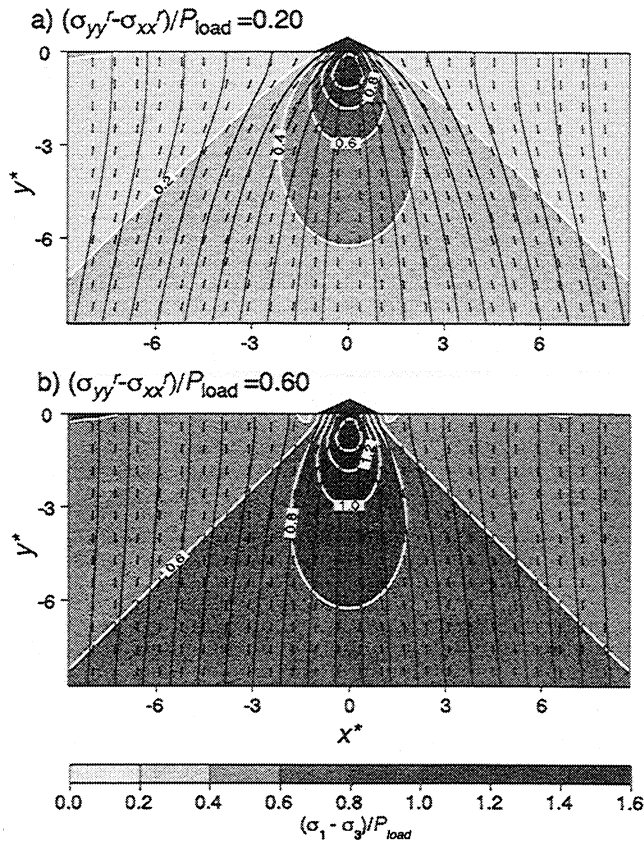
## a) $(\sigma_{yy}{}^r - \sigma_{xx}{}^r)/P_{load} = 0.20$



## b) $(\sigma_{yy}{}^r - \sigma_{xx}{}^r)/P_{load} = 0.60$



$(\sigma_1 - \sigma_3)/P_{load}$

**Figure 8.** Magnitude of scaled differential stress (shaded and contoured), trajectories of the most compressive principal stress (ticks), and potential dike propagation paths (solid lines) beneath a triangular normal load distribution for a constant regional differential stress. Differential stress parameter $(\sigma_{yy}{}^r - \sigma_{xx}{}^r)/P_{load}$ is equal to (a) 0.20 and (b) 0.60.

$$x^*_c = 0.703\left[\frac{(1-k)\rho_0 g l}{P_{load}}\right]^{-0.735} + 1.0, \qquad (10)$$

indicating a nearly inverse relation between $x^*_c$ and the differential stress parameter $(1-k)\rho_0 g l/P_{load}$. Thus the distance of dike attraction is very sensitive to a regional differential stress that increases with depth (i.e., $k < 1$), particularly when the stress state is close to isotropic (i.e., $k \to 1$).

We now consider the alternative possibility that the magnitude of differential stress is constant throughout the lithosphere as might be the case of a uniform tectonic stress. In this case, we define the regional differential stress parameter as $(\sigma_{yy}{}^r - \sigma_{xx}{}^r)/P_{load}$. Figure 8a shows the normalized differential stress field beneath the same volcano load as in Figure 7 but where $(\sigma_{yy}{}^r - \sigma_{xx}{}^r)/P_{load} = 0.20$. The predicted dike trajectories indicate that dikes will be attracted to the volcano from ~5 times the load half width for this case. As the differential stress parameter $(\sigma_{yy}{}^r - \sigma_{xx}{}^r)/P_{load}$ is increased (Figure 8b), stresses and dike trajectories become everywhere more vertical. Increasing the magnitude of $(\sigma_{yy}{}^r - \sigma_{xx}{}^r)/P_{load}$ to 0.60 reduces the extent of dike attraction to approximately two times the load half width.

The predicted dependence of $x^*_c$ on $(\sigma_{yy}{}^r - \sigma_{xx}{}^r)/P_{load}$ is summarized in Figure 9. Similar to the case in which differential stress increases with depth (Figure 7), $x^*_c$ decreases rapidly as $(\sigma_{yy}{}^r - \sigma_{xx}{}^r)/P_{load}$ increases from 0.0 to ~0.5 and decreases more gradually to an asymptotic value of 1.0 for

larger differential stresses. The results are described as follows:

$$x^*_c = 0.846\left[\frac{(\sigma_{xx}{}^r - \sigma_{yy}{}^r)}{P_{load}}\right]^{-0.861} + 1.0, \qquad (11)$$

a scaling law very similar to that for the vertical gradient in differential stress (equation (10)). The similarity between the two equations indicates that in either the case of a depth-dependent (equation (10)) or a constant differential stress (equation (11)), the normalized differential stress at a depth equal to the load half width characterizes the potential of dike attraction. The ability of large volcanoes to attract dikes from a broad area at depth will be greatest when the regional stress state is nearly isotropic. Dikes are attracted from a narrow region where the region differential stress is large relative to the surface load.

## 5. Stresses Due to Flexure of an Elastic Plate

It is widely recognized that the elastic portion of the lithosphere has finite thickness and over long timescales behaves as an elastic plate that bends in response to surface loads [e.g., *McKenzie and Bowin*, 1976; *Banks et al.*, 1977; *Burov and Diament*, 1995, 1996]. Bending of a plate of finite thickness contributes additional stresses that are not considered in our models of an elastic half-space. These stresses may influence magma transport as suggested by an apparent global relationship between volcano spacing and effective elastic plate thickness $T_e$ [*ten Brink*, 1991]. The magnitude of the flexural stresses in the plate increases with load size and decreases with $T_e$. For relatively small loads and thick elastic plates, bending stresses will be small and the dominant source of anisotropic ambient stress will be due to local compression beneath the load, as in our above models. For larger loads and thinner plates, however, bending will be more important.

Here we use thin plate theory to examine the relative magnitudes of bending stresses and the local compressive
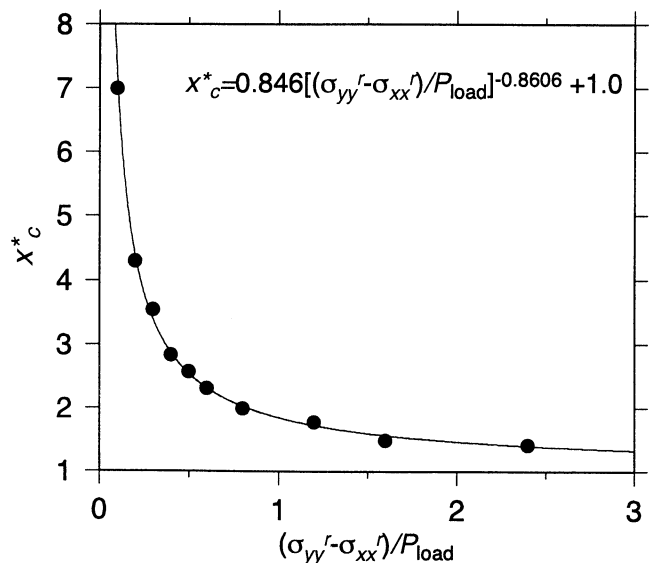


$$x^*_c = 0.846[(\sigma_{yy}{}^r - \sigma_{xx}{}^r)/P_{load}]^{-0.8606} + 1.0$$

$(\sigma_{yy}{}^r - \sigma_{xx}{}^r)/P_{load}$

**Figure 9.** The numerical predictions of $x^*_c$ (dots) decrease with differential stress parameter $(\sigma_{yy}{}^r - \sigma_{xx}{}^r)/P_{load}$ according to the relationship at top (equation (11)).
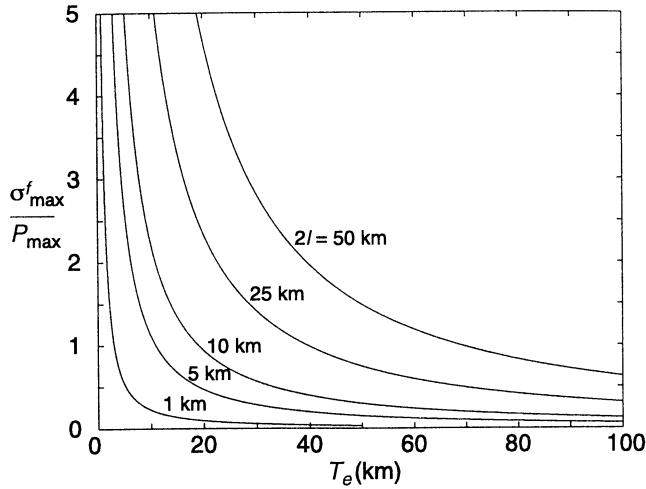
**Figure 10.** Relationship between the ratio of the maximum horizontal stress due to flexure to the maximum stress at the base of the load $\sigma^f_{max}/P_{max}$ and effective elastic thickness of the lithosphere $(T_e)$ for different surface load widths $(2l)$.

stresses due only to volcano loads. The symmetric deflection $w$ of an elastic plate beneath a line load is

$$w = \frac{V_0 \alpha^3}{8D} \exp\left(\frac{-x}{\alpha}\right)\left(\cos\frac{x}{\alpha} + \sin\frac{x}{\alpha}\right), \qquad (12)$$

where $V_0$ is the force per unit length of a surface line load at $x=0$, $D$ is the flexural rigidity

$$D \equiv \frac{ET_e^3}{12(1-v^2)}, \qquad (13)$$

and $\alpha$ is a quantity that defines the flexural wavelength

$$\alpha = \left(\frac{4D}{\Delta\rho_0 g}\right)^{1/4} \qquad (14)$$

*Turcotte and Schubert,* 1982]. In (13), $E$ is Young's modulus, and $\Delta\rho_0$ in (14) is the density contrast between the mantle beneath the plate and the material infilling the downwarp of the plate's upper surface. Since the only load on the surface that we consider is the line load, $\Delta\rho_0 = \rho_0$. This bending generates horizontal stresses in the plate. Their magnitude increases with plate curvature $d^2w/dx^2$ and vertical distance from the midplane $(y =-T_e/2)$ of the plate. At the top and bottom of the plate the horizontal stress magnitudes are greatest with absolute values given by

$$\sigma_{xx}^f = \left|\frac{3V_0\alpha}{2T_e^2}\exp\left(\frac{-x}{\alpha}\right)\left(\sin\frac{x}{\alpha} - \cos\frac{x}{\alpha}\right)\right|. \qquad (15)$$

Where curvature is positive, as it is beneath the load, $\sigma_{xx}^f$ is compressive at the top of the plate and tensile at the bottom of the plate. Directly beneath the load, $\sigma_{xx}^f$ is maximum and equal to

$$\sigma^f_{max} = \frac{3V_0\alpha}{2T_e^2}. \qquad (16)$$

We consider a triangular load with $V_0 =P_{max}l$, where $P_{max} = 2P_{load}$ is the maximum normal force at $x=0$. The ratio between the maximum horizontal stress due to flexure $\sigma^f_{max}$ and $P_{max}$ is

$$\frac{\sigma^f_{max}}{P_{max}} = \frac{3l}{2T_e^{5/4}}\left[\frac{E}{3(1-v^2)\rho_0 g}\right]^{1/4}. \qquad (17)$$

We use this ratio to determine the importance of flexural stresses relative to the local compressive stresses due only to the load. Equation (17) shows that $\sigma^f_{max}/P_{max}$ increases with load half width $l$ and decreases with elastic plate thickness. Values of $\sigma^f_{max}/P_{max}$ for a range of plate thicknesses $T_e$ and applied load half widths are shown in Figure 10. Roughly speaking, when volcano half widths are less than a quarter of the effective elastic plate thickness, loading stresses $P_{max}$ are comparable to or larger than bending stresses. The above results suggest that our model of an elastic half-space is most applicable to regions where small volcanoes load thick and old lithosphere (i.e., $T_e > 4l$). Alternatively, in environments where volcano widths are large compared to the effective elastic plate thickness, our models are only applicable during the early stages of volcano growth when volcanoes are small and/or when anisotropic stresses in the viscous portions of the crust and mantle are still supporting anisotropic stress and are thus contributing to the effective elastic strength of the lithosphere. We also note that flexural stresses will cause dikes to focus toward loads [*Hieronymous and Bercovici,* 1999] and thus influence dike propagation in the same sense as our model.

## 6. Volcano Size and Spacing in the Cascade Range

Our model of volcano loads attracting feeder dikes has two main implications for the evolution of volcanic provinces. First, the direct relationship between volcano size and lateral distance of dike attraction predicts a positive feedback between volcano size and magma supply rate. This positive feedback will selectively favor the growth of large discrete volcanoes over densely spaced small volcanoes. The second implication is that if all magma within a volcano's region of dike attraction only feeds that volcano, then this will limit the growth rate of neighboring volcanoes and/or set a minimum distance at which new volcanoes will form. For example, one possible scenario is that a volcanic province begins with a random distribution of small volcanoes. Those volcanoes that are spaced far apart will be least likely to compete for the magma supply from below and therefore begin to grow faster than volcanoes that are closely spaced. Ideally, the system evolves such that the volcanoes with the greatest spacing will be the largest, and the volcanoes with the closest spacing will be the smallest. We therefore predict a dependence of volcano spacing on volcano size.

Previous studies of arc volcanoes on active continental margins have found that the spacing between volcanoes is fairly uniform within a given province [*Vogt,* 1974; *Marsh and Carmichael,* 1974]. Models to explain a uniform spacing include volcanism through lithospheric fractures with spacing controlled by lithospheric thickness [*Vogt,* 1974], as well as periodic mantle upwellings with spacing controlled by the thickness of the buoyant asthenospheric layer [*Marsh and Carmichael,* 1974; *Davies and Stevenson* 1992]. In contrast, a more recent study, which includes a larger number of volcanoes and greater range of volcano sizes, shows large variations in volcano spacing within several arc volcano provinces [*de Bremond d'Ars et al.,* 1995]. *de Bremond d'Ars*

**Table 2.** Cascade Volcano Data

| Volcano | Lat. | Long. | Edifice Height, m | Diameter, km | Volume, km$^3$ |
|---------|------|-------|-------------------|--------------|----------------|
| Baker | 48.79 | 121.82 | 2500[b] | 26[b] | - |
| Glacier Peak | 48.12 | 121.12 | 1200[a] | - | - |
| Rainier | 46.85 | 121.75 | 2440[a], 2150[b] | 17[a], 18[b] | 270[a] |
| Goat Rocks | 46.5 | 121.45 | 1150[a] | 11[a] | - |
| St. Helens | 46.2 | 122.19 | 1950[a], 1500[b], 1450[c] | 8.5[a], 10.4[b] | - |
| Adams | 46.2 | 121.5 | 2700[a], 1920[c] | - | 200[a] |
| Hood | 45.37 | 121.7 | 2180[a], 1800[c] | - | 50[a] |
| Jefferson | 44.66 | 121.8 | 1675[d] | - | 25[a] |
| Washington | 44.33 | 121.84 | 1200[a] | 5[a] | - |
| Broken Top | 44.08 | 121.7 | 780[a] | 8[a] | - |
| North Sister | 44.17 | 121.77 | 1370[d] | - | - |
| South Sister | 44.1 | 121.77 | 1400[d] | - | - |
| Bachelor | 43.78 | 121.58 | 1460[a] | - | 40[a] |
| Crater Lake | 42.94 | 122.1 | 2400[a, e] | 27[b] | 130[a] |
| Pelican Butte | 42.51 | 122.06 | 1170[a] | - | 20[a] |
| McLoughlin | 42.44 | 122.31 | 1200[a] | - | 13[a] |
| Brown Mountain | 42.36 | 122.27 | 730[a] | - | 5[a] |
| Newberry | 43.68 | 121.25 | 1100[a] | 44[b] | 450[a] |
| Medicine Lake | 41.6 | 121.6 | 1200[a, e] | 40[b] | 600[a] |
| Shasta | 41.4 | 122.18 | 3500[a] | - | 350[a] |
| Lassen | 40.5 | 121.5 | 1907[a], 1380[b], 1130[c] | 12[a], 23[b] | 80[a] |

[a]*Wood and Kienle* [1990].
[b]*Pike and Clow* [1981].
[c]*List of the World Active Volcanoes* [1971].
[d]USGS topographic maps.
[e]Extrapolated values of ancestral volcano.

*et al.* [1995] demonstrated that this large range of spacing is statistically well represented by a random distribution. However, they did not investigate if volcano spacing correlates with volcano size.

To test for a correlation between volcano spacing and size, we now examine volcanoes in the Cascade range of Washington, Oregon, and northern California. Data on volcano width are sparse, presumably because the very gradual slopes of their bases introduce large uncertainties in basal diameters. We therefore use edifice height *h* above the surrounding topography as a measure of volcano size (differences in volcano heights will be proportional to variations in widths to the degree that the volcanoes have similar shapes). In cases that multiple height estimates are cited for a single volcano, we simply use the average value. To ensure that the volcanoes represent significant topographic anomalies we select only those volcanoes with heights exceeding 700 m. We include the pre-1980 height of Mount St. Helens as well as the extrapolated heights of the ancestral volcanoes of Crater Lake and Medicine Lake craters. With these criteria we produce a list of 21 volcanoes (Table 2). Each volcano is paired with its nearest neighbor to produce 14 unique volcano pairs (Table 3). We measure the separation distance between the two volcanoes in a pair and compute the average of their heights.

In Figure 11 we plot spacing and average volcano height for each pair. We use the average height in each volcano pair because both volcanic loads are predicted to control the spacing between them. The first major observation is that volcano spacing varies substantially from as small as 6 km (South Sister-Broken Top) to 115 km (Lassen-Shasta). In fact, the standard deviation of 33.4 km is comparable to the average spacing of 47.9 km. This result is consistent with figures from *de Bremond d'Ars et al.* [1995] for the Cascades. They show a standard deviation comparable to their mean (29.6

km), though their mean is less than ours because they use a larger number of volcanoes. The average spacing in our volcano pairs is significantly less than the average (~80 km) suggested by *Marsh and Carmichael* [1974], but their data set also includes volcanoes from the Aleutian Islands and the Alaska Peninsula. Most importantly, our finding that there is a broad range of spacing is contrary to previous studies that suggest that the spacing is uniform [*Vogt*, 1974; *ten Brink*, 1991]. A uniform spacing would be expected if spacing is controlled by lithospheric flexure [*ten Brink*, 1991; *Hieronymous and Bercovici*, 1999]. The large range in nearest-neighbor spacing that we see suggests that flexure is not the primary factor controlling spacing in the Cascades. Indeed, *ten Brink* [1991] found the Cascades to lie well away from the prediction of his lithospheric flexure model.

The second major observation in Figure 11 is a correlation between volcano spacing and average volcano height. The

**Table 3.** Volcano Spacing Data

| Nearest Volcano Pair | Spacing, km | Average Height, m |
|----------------------|-------------|-------------------|
| Baker-Glacier Peak | 91 | 1850 |
| Rainier-Goat Rock | 45 | 1723 |
| Adams-St. Helens | 53 | 1970 |
| Hood-Adams | 94 | 2150 |
| Jefferson-Washington | 37 | 1440 |
| Washington-North Sister | 19 | 1290 |
| North Sister-South Sister | 8 | 1385 |
| South Sister-Broken Top | 6 | 1090 |
| Bachelor-Broken Top | 35 | 1120 |
| Newberry-Broken Top | 57 | 940 |
| Crater Lake-Pelican Butte | 48 | 1780 |
| Brown Mountain-McLaughlin | 10 | 965 |
| Shasta-Medicine Lake | 53 | 2350 |
| Lassen-Shasta | 115 | 2490 |
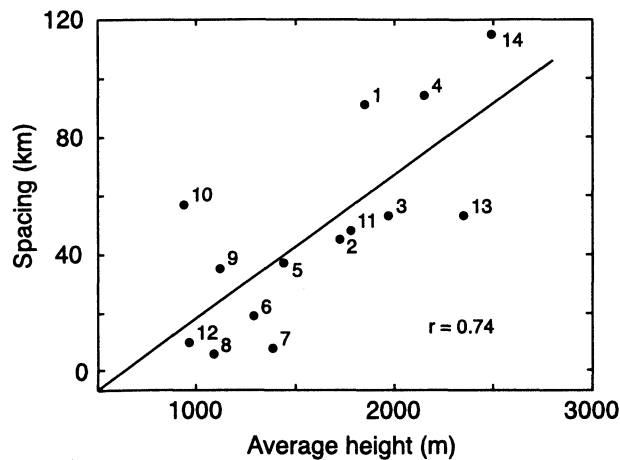
**Figure 11.** Observed relationship between the spacing between nearest-neighbor Cascade volcanoes and the average of their edifice heights. The best fit line has a linear correlation coefficient $r = 0.74$.

best-fit line through the data has a slope of 489 (0.0489 km m$^{-1}$) and a correlation coefficient $r = 0.74$. The quantity $t = [(n\text{-}2)/(1\text{-}r^2)]^{1/2}$, where $n$ is the number of pairs, provides a test for the significance of the correlation [*Swan and Sandilands*, 1995]. The computed value of $t = 3.19$ exceeds the 0.5% significance level of 3.055 [*Swan and Sandilands*, 1995] thereby indicating that the correlation between spacing and average height is significant. The best fit slope is likely to depend on factors that affect the size of the region of dike attraction for each volcano. These factors include the sizes of volcanoes as well as the remote differential stress field. Further modeling efforts are necessary to constrain these relationships. In general, the observed trend is consistent with the prediction of our model that the region of dike attraction will increase with load size. Lithospheric stresses associated with volcanic loads may therefore be an important factor in focusing magma transport in the Cascade region.

On the basis of our comparison of flexure stresses and load magnitude ($\sigma^f_{max}/P_{max}$) the above results suggest that the effective elastic plate thickness beneath the Cascade volcanoes is several times greater than the radii of the volcanoes. If the effective elastic plate thickness is a factor of 4 times the basal radius of 10-15 km for Mount Shasta, then this would suggest an effective elastic plate thickness of the order of 40-60 km. This thickness is several times that estimated by *Bechtel et al.* [1990] ($T_e = 8\text{-}16$ km). The estimate of *Bechtel et al.* [1990], however, was based on coherence between the regional topography and gravity field and therefore includes structure that was formed well before the Cascade volcanoes at a time when the lithosphere was younger and most likely thinner. This estimate may therefore be biased to low values of $T_e$.

Another factor that should be considered is the timescales of volcano loading compared to the viscous response time of the lower crust and mantle. Many Cascade volcanoes such as Mount Shasta, Mount St. Helens, Crater Lake, and Medicine Lake have experienced episodes of growth followed by catastrophic avalanches and sector collapses over periods of 10$^5$ years [e.g., *Crandell et al.*, 1984; *Wood and Kienle*, 1990]. During these periods of loading and unloading, the rheologically weak portions of the crust and lithosphere will support anisotropic stresses and therefore contribute to the

strength of the lithosphere. Calculations by *McGovern and Solomon* [1998] show that the time it takes for these anisotropic stresses to decay is of the order of 10$^3$ $\tau_a$, where $\tau_a = 2(1+v)\eta/E$ is the Maxwell timescale. A viscosity $\eta$ of 10$^{20}$ Pa s and $E = 10^{11}$ Pa suggests a relaxation time of ~10$^5$ years which is also consistent with estimates by *Burov and Diament* [1996]. The viscous portions of the crust and mantle may therefore be contributing to the strength of the lithosphere over an appreciable portion of the growth period of many Cascade volcanoes. Thus effective elastic plate thickness during volcano growth may be larger than the long-term, steady state value.

Finally, we recognize that our simple model omits features such as preexisting faults or material heterogeneities that can affect dike propagation; nor do our models consider the effects of other topographic loads. Indeed, we expect that factors such as these may contribute to the scatter about our linear prediction. In addition, we have only quantified the effects of a single 2-D surface load; therefore the extrapolation of our results to the spacing of many 3-D volcanoes is essentially qualitative. Nonetheless, an apparent dependence of volcano spacing on volcano size (Figure 11) suggests that volcano loading may indeed be a factor controlling magma transport.

## 7. Conclusions

Volcanic surface loading can focus dikes initiated at depth to individual volcanoes over lateral distances proportional to the volcano width and weight and inversely proportional to the driving pressure of dikes. The attraction of dikes toward volcanoes will be most significant where the lithospheric regional stress is nearly isotropic. The region of attraction shrinks as the difference between the vertical and horizontal far-field compressive stress in the lithosphere increases. In addition, our models of an elastic half-space apply most to small volcanoes on thick elastic plates, whereas flexural stresses will be more important when volcano widths exceed the elastic plate thickness by a factor of 4 or more. The predicted influence of volcano size on distance of attraction is a mechanism that promotes a positive feedback between volcano size and growth rate. The above dependence also suggests that the sizes of a volcano will be influenced by the proximity to other volcanoes. Nearest-neighbor pairs of the largest volcanoes in the Cascade range in spacing suggesting that the importance of lithospheric flexure, which predicts uniform spacing, is not applicable in this region. Moreover, the spacing of Cascade volcanoes correlates positively with average height. This correlation supports our model and thus suggests that the local stresses associated with volcano loading is an important factor in controlling magma transport in the Cascade volcano province.

## References

Anderson, E.M., *The Dynamics of Faulting*, 206 pp., Oliver and Boyd, White Plains, N.Y., 1951.

Banks, R.J., R.L. Parker, and S.P. Huestis, Isostatic compensation on a continental scale: local versus regional mechanisms, *Geophys. J. R. Astron. Soc.*, *51*, 431-452, 1977.

Bechtel, T.D., D.W. Forsyth, V.L. Sharpton, and R.A.F. Grieve, Variations in effective elastic thickness of the North American lithosphere, *Nature*, *343*, 636-638, 1990.

Burov, E. B., and M. Diament, The effective elastic thickness ($T_e$) of continental lithosphere: What does it really mean?, *J. Geophys. Res., 100*, 3905-3927, 1995.

Burov, E., and M. Diament, Isostacy, equivalent elastic thickness, and inelastic rheology of continents and oceans, *Geology*, *24*, 419-422, 1996.

Cotterell, B., and J.R. Rice, Slightly curved or kinked cracks, *Int. J. Fract. Mech.*, *16*, 155-169, 1980.

Crandell, D.R., C.D. Mitler, A.X. Glicken, R.L. Christiansen, and C.G. Newhall, Catastrophic debris avalanche from ancestral Mount Shasta volcano, California, *Geology*, *12*, 143-146, 1984.

Crouch, S.L., and A.M. Starfield, *Boundary Element Methods in Solid Mechanics*, Allen and Unwin, Concord, Mass., 1983.

Davies, J.H., and D.J. Stevenson, Physical model of source region of subduction zone volcanics, *J. Geophys. Res.*, *97*, 2037-2070, 1992.

de Bremond d'Ars, J., C. Jaupart, and R.S.J. Sparks, Distribution of volcanoes in active margins, *J. Geophys. Res.*, *100*, 20,421-20,432, 1995.

Decker, R.W., Dynamics of Hawaiian volcanoes: an overview, in *Volcanism in Hawaii*, edited by R.W. Decker, T.L. Wright, and P.H. Stauffer, *U.S. Geol. Surv. Prof. Pap.*, *1350*, 997-1018, 1987.

Delaney, P.T., D.D. Pollard, J.I. Ziony, and E.H. McKee, Field relations between dikes and joints: emplacement processes and paleostress analysis, *J. Geophys. Res.*, *91*, 4920-4938, 1986.

Emerman, S.H., and R. Marrett, Why dikes?, *Geology*, *18*, 231-233, 1990.

Fiske, R.S., and E.D. Jackson, Orientation and growth of Hawaiian volcanic rifts: The effect of regional structure and gravitational stress, *Proc. R. Soc. London*, *329*, 299-326, 1972.

Guffanti, M., and C.S. Weaver, Distribution of late Cenozoic volcanic vents in the Cascade Range: Volcanic arc segmentation and regional tectonic considerations, *J. Geophys. Res.*, *93*, 6513-6529, 1988.

Heimpel, M., and P. Olson, Buoyancy-driven fracture and magma transport through the lithosphere: models and experiments, in *Magmatic Systems*, edited by M.P. Ryan, pp. 223-240, Academic, San Diego, Calif., 1994.

Hieronymous, C.F., and D. Bercovici, Discrete alternating hotspot islands formed by interaction of magma transport and lithospheric flexure, *Nature*, *397*, 604-606, 1999.

Hughes, J.M., R.E. Stoiber, and M.J. Carr, Segmentation of the Cascade volcanic chain, *Geology*, *8*, 15-17, 1980.

Ingraffea, A.R., Theory of crack initiation and propagation in rock, in *Fracture Mechanics of Rock*, edited by B.K. Atkinson, pp. 71-110, Academic, San Diego, Calif., 1987.

Ito, G., S.J. Martel, and D. Bercovici Magma transport in the lithosphere through interacting dikes, *Eos, Trans. AGU, 78(46)*, Fall Meet. Suppl., F694, 1997.

Jaeger, J.C., and N.G.W. Cook, *Fundamentals of rock mechanics*, 593 pp., Chapman and Hall, New York, 1979.

Johnson, K.L., *Contact Mechanics*, 452 pp., Cambridge Univ. Press, New York, 1985.

Lawn, B., *Fracture of Brittle Solids*, 2nd ed., 378 pp., Cambridge Univ. Press, New York, 1993.

List of the World Active Volcanoes, in *Special Issue of Bulletin of Volcanic Eruptions*, edited by Y. Katsui, Volcanol. Soc. of Jpn., Tokyo, 1971.

Lister, J.R., Buoyancy-driven fluid fracture: The effects of material toughness and of low viscosity precursors, *J. Fluid Mech.*, *210*, 263-280, 1990.

Lister, J.R., and R.C. Kerr, Fluid-mechanical models of crack propagation and their application to magma-transport in dykes, *J. Geophys. Res.*, *96*, 10,049-10,077, 1991.

Lister, J.R., The solidification of buoyancy-driven flow in a flexible-walled channel, part I, Constant volume, *J. Fluid Mech.*, *272*, 21-44, 1994.

Marsh, B.D., and I.S.E. Charmichael, Benioff zone magmatism, *J. Geophys. Res.*, *79*, 1196-1206, 1974.

McGarr, A., On the state of lithospheric stress in the absence of applied tectonic forces, *J. Geophys. Res.*, *93*, 13,609-13,617, 1988.

McGovern, P.J., and S.C. Solomon, State of stress, faulting, and eruption characteristics on large volcanoes on Mars, *J. Geophys. Res.*, *98*, 23,553-23,579, 1993.

McGovern, P.J., and S.C. Solomon, Growth of large volcanoes on Venus: Mechanical models and implications for structural evolution, *J. Geophys. Res.*, *103*, 11,071-11,101, 1998.

McKenzie, D., and C. Bowin, The relationship between bathymetry and gravity in the Atlantic Ocean, *J. Geophys. Res.*, *81*, 1903-1915, 1976.

Olson, J.E., and D.D. Pollard, Inferring paleostresses from natural fracture patterns: A new method, *Geology*, *17*, 345-348, 1989.

Olson, J.E., and D.D. Pollard, The initiation and growth of echelon veins, *J. Struct. Geol.*, *13*, 595-608, 1991.

Pike, R.J., and G.D. Clow, Revised classification of terrestrial volcanoes and catalog of topographic dimensions, with new results on edifice volume, *U.S. Geol. Surv. Open File Rep.*, *1038*, 1-40, 1981.

Pollard, D.D., and O.H. Muller, The effects of gradients in regional stress and magma pressure on the form of sheet intrusions in cross section, *J. Geophys. Res.*, *81*, 975-984, 1976.

Pollard, D.D., and P. Segall, Theoretical displacements and stresses near fractures in rock: With applications to faults, joints, veins, dikes, and solution surfaces, in *Fracture Mechanics of Rock*, edited by B.K. Atkinson, pp. 277-349, Academic, San Diego, Calif., 1987.

Rogers, G.C., Variation in Cascade volcanism with margin orientation, *Geology*, *13*, 495-498, 1985.

Rubin, A.M., Dikes vs. diapirs in viscoelastic rock, *Earth Planet. Sci. Lett.*, *119*, 641-659, 1993.

Rubin, A.M., Propagation of magma-filled cracks, *Annu. Rev. Earth Planet. Sci.*, *23*, 287-336, 1995.

Rubin, A. M., Dike ascent in partially molten rock, *J. Geophys. Res.*, *103*, 20,901-20,919, 1998.

Savage, W.Z., H.S. Swolfs, and P.S. Powers, Gravitational stresses in long symmetric ridges and valleys, *Int. J. Rock Mech., Mineral Sci., Geomech. Abstr.*, *22*, 291-302, 1985.

Secor, D.T., and D.D. Pollard, On the stability of open hydraulic fractures in the earth's crust, *Geophys. Res. Lett.*, *2*, 510-513, 1975.

Spence, D.A., and D.L. Turcotte, Magma-driven propagation of cracks, *J. Geophys. Res.*, *90*, 575-580, 1985.

Spence, D.A., and D.L. Turcotte, Buoyancy-driven magma fracture: a mechanism for ascent through the lithosphere and the emplacement of diamonds, *J. Geophys. Res.*, *95*, 5133-5139, 1990.

Swan, A.R.H., and M. Sandilands, *Introduction to Geological Data Analysis*, 446 pp., Blackwell Sci., Malden, Mass., 1995.

Takada, A., Experimental study on propagation of liquid-filled crack in gelatin: Shape and velocity in hydrostatic stress condition, *J. Geophys. Res.*, *95*, 8471-8481, 1990.

Takada, A., Development of a subvolcanic structure by the interaction of liquid-filled cracks, *J. Volcanol. Geotherm. Res.*, *62*, 207-224, 1994.

ten Brink, U., Volcano spacing and plate rigidity, *Geology*, *19*, 397-400, 1991.

Timoshenko, S.P., and J.N. Goodier, *Theory of Elasticity*, 567 pp., McGraw-Hill, New York, 1970.

Turcotte, D.L., and J. Phipps Morgan, The physics of magma migration and mantle flow beneath a mid-ocean ridge, in *Mantle Flow and Melt Generation at Mid-Ocean Ridges, Geophys. Monogr. Ser.*, vol. 71, edited by J.B. Phipps Morgan, D.K. Blackman, and J.M. Sinton, pp. 155-182, AGU, Washington, D.C., 1992.

Turcotte, D.L., and G. Schubert, *Geodynamics: Applications of Continuum Physics to Geological Problems*, 450 pp., John Wiley, New York, 1982.

Vogt, P.R., Volcano spacing, fractures, and thickness of the lithosphere, *Earth Planet. Sci. Lett.*, *21*, 235-252, 1974.

Weaver, C.S., and C.A. Michaelson, Seismicity and volcanism in the Pacific Northwest: Evidence for the segmentation of the Juan de Fuca plate, *Geophys. Res. Lett.*, *12*, 215-218, 1985.

Wood, C.A., and J. Kienle, *Volcanoes of North America, United States and Canada*, 354 pp., Cambridge Univ. Press, New York, 1990.

G. Ito, Department of Geology, University of California, Davis, CA 95616. (gito@geology.ucdavis.edu.)

S. J. Martel, Department of Geology and Geophysics, University of Hawaii at Manoa, Honolulu, HI 96822. (martel@soest.hawaii.edu.)

J. R. Muller, Department of Geological and Environmental Sciences, Stanford University, Stanford, CA 94305-2115. (mullerj@pangea.stanford.edu.)